doi:10.26443/seismica.v4i1.1471

SEISMICA

Characterization and validation of tidally calibrated strains from the Alto Tiberina Near Fault Observatory Strainmeter Array (TABOO-NFO-STAR)

C. Hanagan *[1,*], **E. Mandler** [2], **R. A. Bennett** [1,x], **L. Chiaraluce** [2], **M. Gottlieb**[3], **A. Gualandi** [2,4], **A. Hughes** [1], **W. Johnson**[3], **D. Mencin**[3], **S. Marzorati** [2]

[1]Department of Geosciences, The University of Arizona, Tucson, AZ, USA, [2]Istituto Nazionale di Geofisica e Vulcanologia, Rome, Italy, [3]EarthScope, USA, [4]Department of Earth Sciences, University of Cambridge, UK, [*]Now at the U.S. Geological Survey, Earthquake Science Center, Golden, CO, USA, [x]Now at NOAA National Geodetic Survey, Silver Spring, MD, USA

Author contributions: *Conceptualization*: C. Hanagan, E. Mandler, R.A. Bennett, L. Chiaraluce, M. Gottlieb, A. Hughes. *Funding Acquisition*: R.A. Bennett, L. Chiaraluce, D. Mencin. *Field Installation*: C. Hanagan, E. Mandler, R.A. Bennett, L. Chiaraluce, M. Gottlieb, A. Gualandi, W. Johnson, D. Mencin, S. Marzorati. *Methodology*: C. Hanagan, E. Mandler. *Formal Analysis*: C. Hanagan, E. Mandler, M. Gottlieb. *Supervision*: R. Bennett, A. Hughes. *Writing – original draft*: C. Hanagan. *Writing – review & editing*: C. Hanagan, E. Mandler, R.A. Bennett, L. Chiaraluce, M. Gottlieb, A. Gualandi, A. Hughes, W. Johnson, D. Mencin, S. Marzorati.

Abstract Six horizontal borehole tensor strainmeters (TSM1-6) installed from Fall 2021 to Spring 2022 comprise the Alto Tiberina Near Fault Observatory Strainmeter Array (STAR), providing an unprecedented opportunity to investigate seismic and aseismic deformation from hazardous high- and low-angle normal faults in Italy. Prior to use in tectonic applications, they require in-situ calibration and correction for non-tectonic signals. We tidally calibrate the instruments, characterize the calibration uncertainty, and test the results against environmental and earthquake signals originating from local to teleseismic distances. The STAR sites demonstrably deviate from assumptions common to the standard manufacturer's calibrations, including negative areal coupling at TSM3-6. While the tidally calibrated strains have ~3-56% uncertainty, the calibrated dynamic strains show interstation precision and accuracy to nanostrain levels, and static coseismic offsets in the array footprint are within uncertainty. TSM3 records a complex series of strains that may arise from dynamically triggered near-borehole fracture slip and fluid flow that does not appear to affect its sensitivity to lower strain rate deformation. Future calibration improvement may be afforded with longer stable timeseries, particularly for TSM4. Overall, our analyses demonstrate expanded geodetic capability for detecting deformation in the Alto Tiberina Near Fault Observatory.

Production Editor:
Yen Joe Tan
Handling Editor:
Mathilde Radiguet
Copy & Layout Editor:
Hannah F. Mark

Received:
September 27, 2024
Accepted:
April 30, 2025
Published:
June 2, 2025

1 Introduction

Borehole strainmeters (BSMs) excel in detecting subtle deformation, approaching nanostrain (parts-per-billion) sensitivity over sub-seconds to monthly timespans—bridging the gap between capabilities of more common geodetic and seismic methods (Gladwin, 1984). As such, the instruments are installed throughout several active tectonic regions globally to detect transient deformation that falls below the threshold of more common measurement techniques (e.g. Hodgkinson et al., 2013; Linde et al., 1996; Mandler et al., 2024). Six 4-component horizontal Gladwin Tensor BSMs (Gladwin, 1984) were installed in the Alto Tiberina Near Fault Observatory (TABOO-NFO) of Italy from September 2021 to June 2022 as part of the internationally collaborative STrainmeter ARray (STAR) project, designed to detect low-magnitude, spatiotemporally variable creep in the extending northern central Apennines (Figure 1; Chiaraluce et al., 2024). In this region, geologic, geodetic, and seismologic observations indicate that the ~60 km long, low-angle (<20°) Alto Tiberina normal fault (ATF) creeps below 4 km depth at a rate of ~1.7 +- 0.3 mm/yr (Anderlini et al., 2016). High angle synthetic and antithetic normal faults host part of the remaining 1-2 mm/yr extension, with aseismic slip and moderate magnitude earthquakes in recent history (Chiaraluce et al., 2014; Gualandi et al., 2017). The spatiotemporal variation of creep on sub-monthly timescales remains unknown due to the limited geodetic resolution and precision available to previous studies (Anderlini et al., 2016; Chiaraluce et al., 2007; Mirabella et al., 2011; Valoroso et al., 2017; Vuan et al., 2020; Hreinsdottir and Bennett, 2009). Therefore, the newly installed array presents an unprecedented opportunity to directly measure the details of low-magnitude strain accommodated in the region (Chiaraluce et al., 2024). However, before accurate and precise measurement of strain from fault slip or other phenomena, the data require regional calibration and quality assessment, which remains the pursuit of this study.

Notably, although an extensive network of the same instruments exists in the western United States as part of the Network of the Americas (NOTA; https://www.unavco.org/nota/), they remain underutilized in

*Corresponding author: chanagan@usgs.gov

studies of active tectonic deformation. This may partly result from their high sensitivity to non-tectonic sources of strain, which complicates analysis, but also from lack of accurate calibration (e.g., Langbein, 2010; Roeloffs, 2010; Canitano et al., 2017), unknown uncertainty in the resulting calibrated strain data (e.g. Langbein, 2010, 2015), and/or unclear near-borehole effects or heterogeneities that alter the strain field (e.g. Barbour et al., 2014; Barbour, 2015; Guangyu et al., 2011; Wang and Barbour, 2017; Canitano et al., 2013). Our approach for calibration and validation is designed to help clarify the analysis and interpretation of signals from these stations, which may extend more broadly to other BSMs in active tectonic regions globally.

Various strategies exist to address the problem of accurately calibrating the BSMs (e.g. Hart et al., 1996; Roeloffs, 2010; Hodgkinson et al., 2013; Currenti et al., 2017; Canitano et al., 2017). The Gladwin tensor-type strainmeters consist of four vertically stacked, horizontal strain gauges at different orientations to enable measurement of the full horizontal plane strain tensor (Figure 2; Hart et al., 1996). Standard manufacturer's calibrations, common to the Network of the Americas (NOTA) BSMs (Hodgkinson et al., 2013), account for the coupled strainmeter-borehole-grout system response to rock formation strain, with presumed relative grout-to-bedrock strengths and known gauge orientations. Noted deviations from the manufacturer's calibrations include variable response factors per gauge (Roeloffs, 2010), poorly known gauge azimuths (Hodgkinson et al., 2013; Roeloffs, 2010), sensitivity to vertical strain (Roeloffs, 2010), different strengths between the bedrock and grout (Gladwin and Hart, 1985), topographic influence (Beaumont and Berger, 1975), rock anisotropy, and variable lithology between the stacked gauges, among other near-gauge heterogeneities. Given these complications, other reference signals provide a basis for alternative calibration, including seismic waves (Currenti et al., 2017; Grant and Langston, 2009), comparison with collocated laser strainmeter measurements (Hart et al., 1996; Langbein, 2010; Beaumont and Berger, 1975), and tides (Hart et al., 1996; Hodgkinson et al., 2013; Roeloffs, 2010; Canitano et al., 2017).

The STAR sites reside in carbonates, marls, and turbiditic sandstones, with variable topography and a poorly constrained gauge orientation at TSM4 where the magnetometer used to find the instrument orientation failed. Given the severe deviation from what is expected for the manufacturer's calibrations, and the absence of independent measurements of the strain field, we calibrate the instruments using oscillatory tidal signals observed in the strain record (Hodgkinson et al., 2013). The Earth tides provide a valuable source for calibrating the BSMs because they are generally well-known given our knowledge of Earth's structure and response to tidal forcings, particularly far inland from large bodies of water (Farrell, 1972, 1973). Knowing this, we adopt the non-constrained tidal calibration approach originally presented in Hodgkinson et al. (2013) for the NOTA BSMs. We expand the method to allow for more thorough quantification of uncertainty associated with the inversion, which has not previously been determined for similar instrument calibrations. Even so, the uncertainties and precision of the modeled tides may be substantial enough to affect calibration accuracy (up to 10-30%, Langbein, 2010, 2015). Therefore, we test the calibration quality against (1) environmental signals, (2) little-investigated, directionally polarized low-frequency body wave strains, and (3) static coseismic strain offsets from four earthquakes ranging from distances of 10 to 2000 kms. We also compare our calibration results with results from the alternative tidal calibration approach adopted in Mandler et al. (2024).

Through calibration, uncertainty quantification, and calibrated signal validation, we highlight the necessity of site-specific signal characterization with consideration for ambient strains unrelated to tectonic deformation, and demonstrate the utility of the instruments for enhancing observational potential in the TABOO-NFO.

2 Methods

We briefly describe our calibration workflow, which follows the non-constrained approach of Hodgkinson et al. (2013), reformatted to enable uncertainty quantification. Then, we describe our analysis of static and dynamic earthquake signals to characterize the response of the stations and the validity of the tidal calibrations.

2.1 Data processing, tidal calibration, and uncertainty

We select the longest continuous time series without gaps >1 hr (Figure 3; Table S1), linearize the data to gauge strain from raw gauge counts, correct the time series for offsets (Figure S1), and estimate the M2 and O1 tidal constituent amplitudes and phases from each gauge time series using Baytap08 (Table S2 Tamura and Agnew, 2008; Tamura et al., 1991). Baytap08 uses a Bayesian modeling approach to estimate tidal constituents and other variations correlated with external data (Tamura and Agnew, 2008; Tamura et al., 1991). The M2 and O1 constituents, at periods of 12.42 and 25.81 hrs, respectively, are preferred over other tidal constituents because they have large amplitudes outside of the thermally influenced, pure diurnal and semidiurnal periods that could bias the observed amplitude and phase estimates (Hodgkinson et al., 2013). A barometric pressure coefficient is simultaneously estimated for each gauge during the Baytap08 analysis using the surface pressure sensor data (Table S3).

We then forward model the east/north oriented M2 and O1 tidal amplitudes and phases using the SPOTL (Some Programs for Ocean Tide Loading; Agnew, 2012) program NLOADF (Table S2). The Green's functions for the model use the elastic Earth structure of Harkrider (1970), as calculated in Farrell (1973). For ocean loads, we adopt the TPXO7.2 global model modified by the OSU regional Mediterranean model (Egbert and Erofeeva, 2002); although, this far inland (~60 km from the coast), the STAR sites should be relatively insensitive to the ocean load. This is verified by laser strainmeter measurements ~130 km to the southeast near Gran Sasso

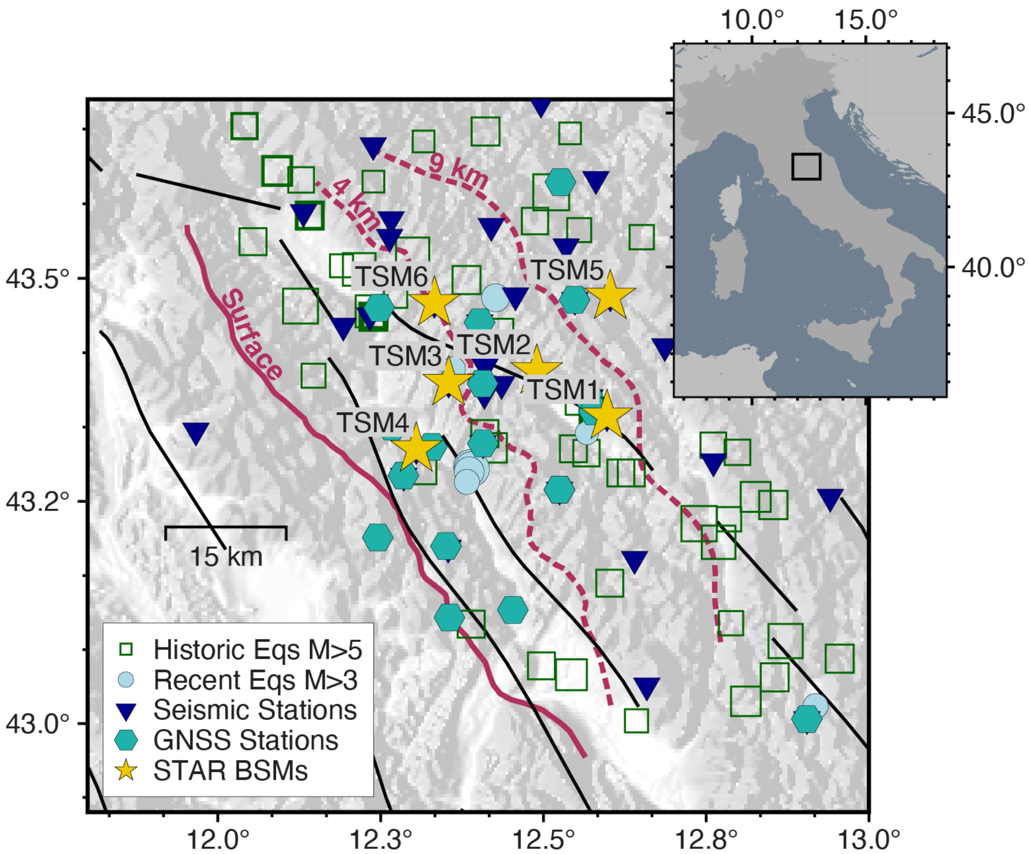

Figure 1 Map of the Alto Tiberina Near Fault Observatory (TABOO-NFO; Chiaraluce et al., 2014), showing historic earthquakes (>M 5) and instrumentally recorded earthquakes (M > 3) scaled by magnitude from October 2021 to June 2023 (INGV), GNSS (Global Navigation Satellite Systems) stations, seismic stations, CO2 sensors, and STrainmeter ARray Borehole Strainmeter (STAR BSM) locations (Bailo et al., 2023). The Alto Tiberina Fault (ATF) contours at the surface, 4 km depth, and 9 km depth are colored in maroon (Mirabella et al., 2011), with simplified black surface regional fault traces overlying the Shuttle Radar Topography Mission topographic hillshade (Farr, 2007).

that demonstrate the ocean tides have at least an order of magnitude less effect on the strain amplitudes than the more predictable solid Earth body tide (Amoruso and Crescentini, 2009).

The calibration matrix of interest contains coefficients that describe the coupling of each gauge to some combination of the areal (e_A), differential shear (e_D), and engineering shear (e_S) strain fields, defined in the east/north reference system as e_{EE}+e_{NN}, e_{EE}-e_{NN}, and 2e_{EN}, respectively (Figure 2). We assume no a priori constraints on the coupling coefficients, and use the observed and modeled tidal constituents to solve for the calibration matrix. Following the non-constrained inversion approach of Hodgkinson et al. (2013), the initial forward problem that matches the observed M2 and O1 tides to the modeled tides takes the form:

$$\begin{bmatrix} e_0^{M_2,Re} & e_0^{M_2,Im} & e_0^{O_1,Re} & e_0^{O_1,Im} \\ e_1^{M_2,Re} & e_1^{M_2,Im} & e_1^{O_1,Re} & e_1^{O_1,Im} \\ e_2^{M_2,Re} & e_2^{M_2,Im} & e_2^{O_1,Re} & e_2^{O_1,Im} \\ e_3^{M_2,Re} & e_3^{M_2,Im} & e_3^{O_1,Re} & e_3^{O_1,Im} \end{bmatrix} = \begin{bmatrix} a_{0A} & a_{0D} & a_{0E} \\ a_{1A} & a_{1D} & a_{1E} \\ a_{2A} & a_{2D} & a_{2E} \\ a_{3A} & a_{3D} & a_{3E} \end{bmatrix} \begin{bmatrix} e_A^{M_2,Re} & e_A^{M_2,Im} & e_A^{O_1,Re} & e_A^{O_1,Im} \\ e_D^{M_2,Re} & e_D^{M_2,Im} & e_D^{O_1,Re} & e_D^{O_1,Im} \\ e_E^{M_2,Re} & e_E^{M_2,Im} & e_E^{O_1,Re} & e_E^{O_1,Im} \end{bmatrix} \quad (1)$$

Where a_{ij} is the coupling matrix, $e_{0\text{-}3}$ denotes the four gauge's real and imaginary parts of the M2 and O1 tidal constituents from the Baytap08 analysis, and $e_{A,D,E}$ denotes the regional areal, differential, and engineering shear strains for the same tidal constituents modeled with SPOTL (Table S2). The Moore-Penrose pseudoinverse of the coupling matrix is the desired calibration matrix, applied to the linear gauge strains to attain the regional strains. We select this non-constrained approach, as opposed to solutions using gauge orientation and coupling coefficient constraints (Hodgkinson et al., 2013), because it allows us to quantify the covariance of the coupling matrix, which we propagate into an estimate of aleatoric uncertainty for the regional strain solutions.

We reformat the inverse problem of equation 1 (Hodgkinson et al., 2013) for standard least squares, where the coupling matrix is sorted into the model vector (m), and the observed data into the data vector (d). The modeled tidal constituents are contained in a block

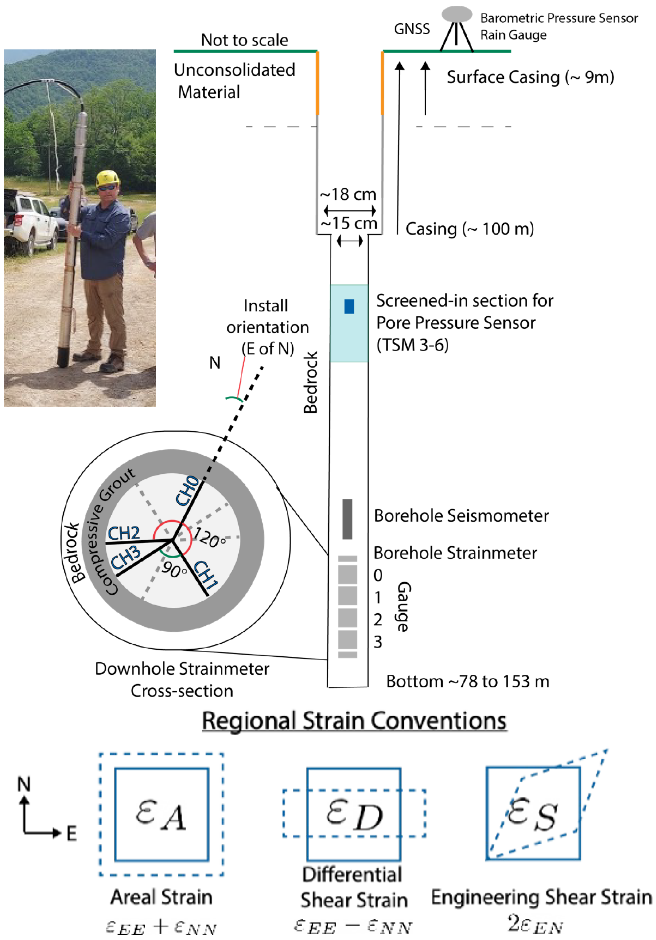

Figure 2 Schematic of a borehole strainmeter (BSM) station with main accompanying instrumentation labeled. The Gladwin Tensor Strainmeter instrument is installed near the bottom of the borehole in competent bedrock with expansive grout to ensure proper coupling to formation strains. Above the strainmeter are a borehole seismometer, screened in section with pressure sensor (at TSM3 through TSM6), and surface GNSS station. A top view representation of the four-gauge (CH0-4 indicates the channel corresponding to a single gauge) linear extensometers is shown on the left. The gauge strains can be transformed into regional areal and shear strains in the east/north reference system, with strain conventions noted at the bottom. In the top left, W. Johnson is pictured with BSM station TSM5 prior to install.

diagonal matrix (G):

$$d = Gm \tag{2}$$

An example expansion of equation 2 for one gauge appears as follows:

$$\begin{bmatrix} e_0^{M_2,Re} \\ e_0^{M_2,Im} \\ e_0^{O_1,Re} \\ e_0^{O_1,Im} \\ \vdots \end{bmatrix} = \begin{bmatrix} e_A^{M_2,Re} & e_D^{M_2,Re} & e_E^{M_2,Re} & \dots \\ e_A^{M_2,Im} & e_D^{M_2,Im} & e_E^{M_2,Im} & \dots \\ e_A^{O_1,Re} & e_D^{O_1,Re} & e_E^{O_1,Re} & \dots \\ e_A^{O_1,Im} & e_D^{O_1,Im} & e_E^{O_1,Im} & \dots \\ \vdots & \vdots & \vdots & \ddots \end{bmatrix}_{16x12} \begin{bmatrix} a_{0A} \\ a_{0D} \\ a_{0E} \\ \vdots \end{bmatrix}_{12x1} \tag{3}$$

The m matrix of calibration coefficients can be reformatted to a 4x3 matrix to match equation 1, resulting in the coupling matrix. The solution to the inverse problem, with weights from the estimated uncertainties from Baytap08 (Table S2), is calculated by generalized weighted least squares (Menke, 2014):

$$m = \left(G^T W G\right)^{-1} G^T W d \tag{4}$$

We found that weighted calibrations produced similar results to those computed without weights, so we complete the inversion with equal weighting on all constituent values to remain consistent with the standard workflow applied to the NOTA BSMs (Hodgkinson et al., 2013). With this modified strategy, we can still estimate an uncertainty for the derived regional strains, which has not been previously calculated for similar tidal calibrations, and can serve as a basis for calibration uncertainty moving forward. We compute the model covariance matrix (C_m) as follows:

$$C_m = \sigma^2_{post} \left(G^T G\right)^{-1} \tag{5}$$

Where $\sigma^2_{post}$is the *a posteriori* variance from the sum of squared residuals (d – Gm) divided by the degrees of freedom, which in this case is 4 given the 12 model parameters less the 16 data observations provided to constrain the solution.

Although the uncertainties in the estimates of the coupling terms are provided via the model covariance, application of the Moore-Penrose inversion eliminates a direct estimate of the uncertainties in the calibration matrix. This is overcome through the simulation of thousands of plausible calibration matrices. We use the model covariance (C_m) to estimate a percentage uncertainty for the calibrated regional strains. To do so, we create 1000 coupling matrices from a multivariate normal distribution described by covariance (C_m) sampled about the nominal coefficient estimates (m), and solve for the calibration matrices from the Moore-Penrose pseudoinverses of the coupling matrices. We then produce a range of regional strain values from 500 random uniform distributions of east, north, and east-north shear strains ranging from -100 to 100 nanostrain. We apply the nominal coupling matrices to these regional strain combinations to retrieve corresponding gauge strain combinations. Then, we recalculate the regional strains from the 500 random gauge strain combinations using the 1000 plausible tidal calibrations,

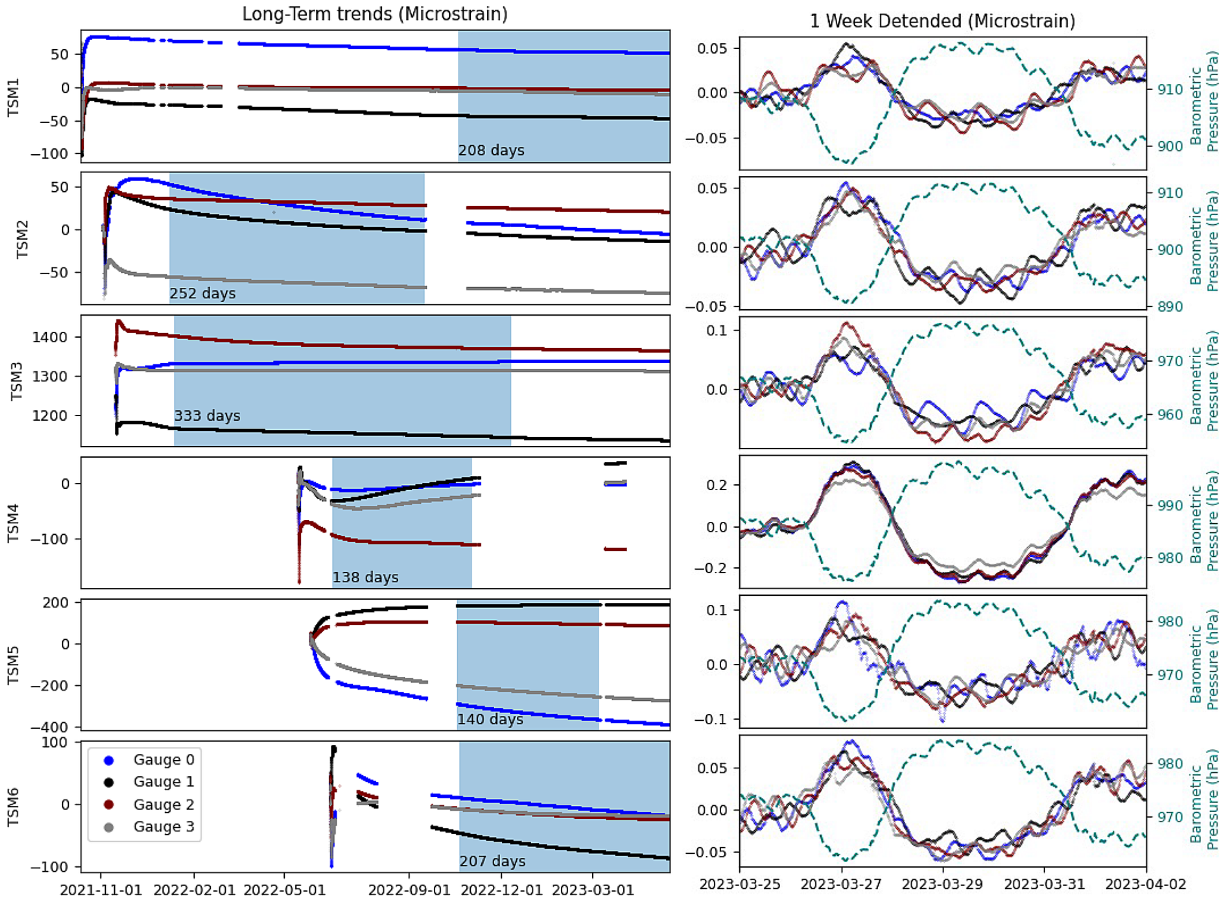

Figure 3 (Left) Linearized gauge strain for the 6 STAR BSMs, demonstrating the transition from initial grout curing after installation to a relatively stable borehole relaxation trend. The processing window for tidal calibration at each station is highlighted in blue and labeled by the number of days (Table S1). The time series are chosen to avoid large gaps of missing data. (Right) Linearized, detrended gauge strain with the barometric pressure at each station for one week in the spring of 2023. The oscillatory diurnal and semi-diurnal tidal signal and compressional gauge response to increased barometric pressure dominate the detrended signal on this timescale.

and determine the percentage difference of the random strain value from the nominal value (i.e. |[random-nominal]/nominal|*100). From these 500,000 percentage differences, we determine the trimmed mean of the percentages after discarding the outlier 32% of values. This provides an estimate of calibration uncertainty as a percentage of the nominal strain value at the level of one standard deviation (68%) for the regional strain components at each station, and minimizes the effect of very large percentages when the regional strain approaches 0. We tested that this percentage is insensitive to the range of random strain values, and stable for the number of perturbed calibrations within 3% of the values reported later.

We also derive strains using the standard manufacturer's calibrations for comparison with the tidal calibrations. A more thorough description of the calibrations is provided in Supplemental Text A. Supplemental Text B introduces the tidal calibrations calculated according to the slightly different methodology of Mandler et al. (2024) that can be completed for instruments without prior dimension information (e.g. instrument diameter), thus skipping the linearization step (Supplemental Text A). The processing and calibration workflow with the calibrations presented here are now implemented in the Earthscopestraintools python package (Gottlieb and Hanagan, 2024, https://earthscopestraintools.readthedocs.io/en/latest/notebooks/TidalCalibrationEarthscopestraintools.html), which can guide future re-calibration as longer time spans of clean data become availab.

2.2 Dynamic strain analysis

As one test of the calibrations, we determine the stations' responses to coseismic, low frequency compressional waves from two earthquakes: the regional Mw 5.5 offshore Ancona, Italy thrust event that occurred on November 9th, 2022 at a distance of ~90 km from STAR, and the devastating Mw 7.8 Kahramanmaras, Turkey strike-slip earthquake that occurred on February 6th, 2023 at a teleseismic distance of ~2000 km away (Tables S4). We perform this analysis based on the preliminary observation that the seismic waves exhibit maximum extension or compression aligned with the event azimuth, matching the sign of expected strain from the event radiation pattern, and providing an independent check on inter-station consistency and calibration success. TSM4 was not recording data during either event, so we omit it in this analysis.

We identify the times, amplitudes, and directions of maximum strain at each station for three low-frequency waves after low-pass filtering the time series below 0.2 Hz with a 4^{th} order Butterworth filter. The prominent oscillations overprint higher frequencies in the strain record (Figure S2). In the case of the Mw 5.5 Ancona earthquake, one signal is identified, roughly coincident with the arrival of the P wave at collocated borehole seismometers, though the exact arrival time of the emergent signal is ambiguous (Figure S2). For the Mw 7.8 Kahramanmaras event, two signals are identified as the P and PP waves. Both P waves have half periods of ~ 5 seconds, and the larger amplitude PP wave has a half period of ~ 9 seconds. Figure S2 plots an example of the signals for the 20 Hz strains overlain with the filtered strains. We apply the calibration matrix to the filtered time-series to derive regional areal, differential, and shear strains, and decompose the regional strains into the east, north, and east-north shear components of the plane strain tensor. We then calculate the principal strain magnitudes and directions for the duration of the signal through eigenvalue decomposition, and find the times, amplitudes, and directions of the principal axes for peak compression or extension.

2.3 Static coseismic strain analysis

To assess the static coseismic response of the stations, we perform simple forward models of fault slip using the event magnitudes, locations, and orientations from focal mechanism plane solutions for the Mw 5.5 Ancona and Mw 7.8 Kahramanmaras earthquakes, in addition to two local events: the March 9^{th}, 2023, Mw 4.3 and 4.5 Umbertide foreshock-mainshock pair that occurred four hours apart within the STAR footprint (Table S4).

The static coseismic offsets are calculated from the unfiltered 20 Hz gauge strains as the average spanning 1 to 2 minutes after the start time of the Umbertide events, 6 to 8 minutes after the Ancona event, and 30 to 60 minutes after the Kahramanmaras event to avoid large variations in dynamic strain. For the near field Umbertide earthquakes, this incorporates some postseismic deformation, though very little considering the short span of time following the event. Given the longer time window for the Kahramanmaras earthquake, we also correct the time series for tides, and note that adjusting the averaging window makes little difference for the far field events because no postseismic deformation is observed at this distance. Figure S3 shows an example of the offset calculation for the Umbertide Mw 4.5 and Kahramanmaras Mw 7.8 events at TSM2.

We forward model fault slip with uniform half-space solutions to compare with the observed coseismic offsets (Okada, 1985). The sources are modeled as single rectangular patches with strike, dip, and rake from time domain moment tensor solutions for the Ancona and Umbertide events (Scognamiglio et al., 2006), and the Global Centroid-Moment-Tensor project solution for the Kahramanmaras earthquake (Table S4; Dziewonski et al., 1981; Ekström et al., 2012). The patch dimensions are scaled to moment magnitude with typical rupture area (A) and width relations for subsurface faults (Wells and Coppersmith, 1994). Slip magnitude (d) is adjusted accordingly to seismic moment (m_0), shear modulus of (μ), and rupture area (d = $m_o A^{-1} \mu^{-1}$). At these distances, the stations are insensitive to the patch aspect provided that the magnitude is preserved, which we confirmed through simple tests at various rupture length and width ratios. We adopt a Poisson's ratio of 0.246, and shear modulus of 32 GPa for the Green's function calculations, calculated from the velocity structure of Harkrider (1970) used for the modeled tides.

3 Results

Here, we assess the nominal tidal calibration results and uncertainty, presented in Table 1, and focus on the retrieval of tidal amplitudes and phases in the context of common coupling assumptions. Then, we present the results for the tidally calibrated responses to 3 types of signals: (1) barometric pressure and rainfall, (2) dynamic strains from the low-frequency coseismic body waves, and (3) static coseismic offsets.

3.1 Tidal calibration results

Baytap08 analysis suggests high signal-to-noise for identifying the amplitudes and phases of the M2 and O1 tides for most stations (Table S2). Gauge 4 at TSM1 is one exception, with a phase uncertainty on the order of magnitude of the result (7±"7°; Table S2). Likewise, Gauges 1 and 4 at TSM4 have relatively poor phase identification for either or both M2 and O1.

The regionally calibrated tidal amplitudes and phases are compared with the predicted tides in the polar plots of Figure 4, and presented in Table S2. At all sites, we calculate Root Mean Square Errors (RMSE) between the calibrated observed (e_{ij}) and predicted (e^*_{ij}; where $i = j = 4$) real and imaginary tidal components, as follows, to compare with results from Hodgkinson et al. (2013):

$$RMSE = \sqrt{\frac{\sum_{i=1}^{i=4} \sum_{j=1}^{j=4} \left(e_{ij} - e^*_{ij}\right)^2}{16}} \tag{6}$$

The RMSEs range from 0.12 to 0.67, with the best fit achieved at TSM2, and poorest fit at TSM4. Hodgkinson et al. (2013) considered an RMSE of <0.84 as indication that the modeled tides are an acceptable reference signal, which all STAR sites achieve (Table S5). We also separate the amplitude and phase RMSEs for each station, presented in Table S5. The amplitude RMSEs range from 0.07 to 1.31 nanostrain, with the best fits achieved at TSM2, and the worst at TSM4. Likewise, these stations have lowest and highest phase RMSEs, at 2.49 and 16.55 degrees, respectively. Except for TSM4, amplitudes are matched within 10% and 20% for the M2 and O1 tides, respectively. Phases are within 5 degrees for the M2 tides at all but TSM4, and within 10 degrees for the O1 tides at all but TSM4 and the differential strains at TSM1 and 6. This indicates some error in either the modeled

	Component	Calibration Matrix				1-standard deviation percentage uncertainty
TSM1	Areal	2.47	3.17	0.78	2.16	27
	Differential	-0.05	-1.65	-0.12	0.13	10
	Engineering	1.94	1.85	-0.42	1.07	22
TSM2	Areal	1.48	2.97	1.79	1.54	14
	Differential	-0.86	0.07	-0.06	-0.62	4
	Engineering	-0.11	0.72	1.32	0.71	7
TSM3	Areal	-0.09	-3.53	-1.66	-2.32	44
	Differential	0.28	0.99	-0.15	0.21	10
	Engineering	-0.41	-1.09	-0.52	-1.00	20
TSM4	Areal	-0.98	-1.89	-1.87	-0.89	58
	Differential	1.17	0.06	-0.11	0.65	26
	Engineering	-0.08	-0.22	-1.49	-0.76	41
TSM5	Areal	-2.30	-1.79	-1.91	-0.24	25
	Differential	-0.08	0.27	0.37	-0.13	3
	Engineering	-0.48	-0.38	-0.01	0.08	6
TSM6	Areal	-4.17	-2.75	-3.75	1.07	46
	Differential	-0.28	-0.14	0.65	0.15	5
	Engineering	0.33	-0.33	-0.15	0.29	5

Table 1 Calibration results for each station, with associated calibration percentage uncertainty at the level of one standard deviation.

tides or the retrieved amplitudes and phases, particularly for the O1 tidal constituent.

Beyond the RMSE results, we can quantify an average percentage uncertainty at the level of one standard deviation for the regional strains considering the model covariance matrix from the inversion (equation 5). Figure 5 and Table 1 show the results of 500 random regional strain combinations calibrated with 1000 perturbed calibrations. The trimmed 1-standard deviation mean of the percentage differences for each component are generally stable for a range of possible strain values, thus we consider them a convenient descriptor of tidal calibration uncertainty. We tested larger ranges of strain and found similar results. The areal strains tend to have the highest uncertainties, in the range of 14-58%, and the differential shear strains tend to have the lowest uncertainties from 3-26%. TSM2 overall has the lowest uncertainty, while TSM4 has the highest, at >26% for all regional strain components (Figure 5).

For comparison with the alternative weighted calibrations, and the standard manufacturer's calibrations, we compute the Root Mean Square difference between the alternative calibration's coupling matrix and preferred unweighted tidal calibration matrix (A_M and A_T^{-1}) with the identity matrix (I) as defined in Hodgkinson et al. (2013); abbreviated RMSI):

$$RMSI = \sqrt{\frac{\sum_{i=1}^{i=3}\sum_{j=1}^{j=3}\left(A_T^{-1}A_M - I\right)^2}{9}} \tag{7}$$

An RMSI of zero indicates good agreement between the two matrices, because the coupling and calibration matrices are inverses of one another. The weighted calibration results, which consider the Baytap08 amplitude and phase uncertainties, are presented in Table S6 with associated RMSE. The weighted calibrations are similar to the non-weighted calibrations for all stations but TSM4, with low RMSI values below 0.06. TSM4, has an RMSI of 0.24, but this is expected given the poor data and calibration quality; thus, we remain consistent with the non-constrained inversion of Hodgkinson et al. (2013) and proceed with the unweighted results as the preferred calibrations. The RMSI values for the manufacturer's and unweighted, preferred calibrations range from 1.85 and 2.86, indicating large differences between the calibrations nearing a factor of 2. The magnetometer at TSM4 failed, so there is no recorded gauge orientation and we omit it in this calculation. The high RMSIs with the Manufacturer's matrices indicate the gauge orientations, gauge coupling, and/or isotropic assumptions of the manufacturer's calibrations likely fail to represent formation strains at these sites.

Exploring this result further, we perform gauge consistency checks for the M2 and O1 tidal amplitudes, where the relationships for gauge combinations ½(e_1+e_3) = ce_A = 2/3(e_0+e_1+e_2) and 2/3(2e_1-e_0-e_2) = de_D = ½(e_1-e_3) should hold true in isotropic conditions with equally sensitive gauges and accurate tidal amplitude and phase estimates (Roeloffs, 2010). However, the gauge combinations are not consistently equal for any station in both tidal bands (Figure S4). Taken together, these results highlight departure from isotropic assumptions and/or equal gauge response to formation strains if the tidal amplitude and phase estimates from the data are approximately correct, as indicated by low standard deviations (Table S2). Similar deviation from the isotropic case was found for several NOTA stations (Roeloffs, 2010; Hodgkinson et al., 2013).

Assuming the orientations recorded at the time of installation are correct, we can calculate coupling coefficients for each gauge from our calibrations for further qualitative description (Tables S7). The areal and shear coupling coefficients are expected to lie in the

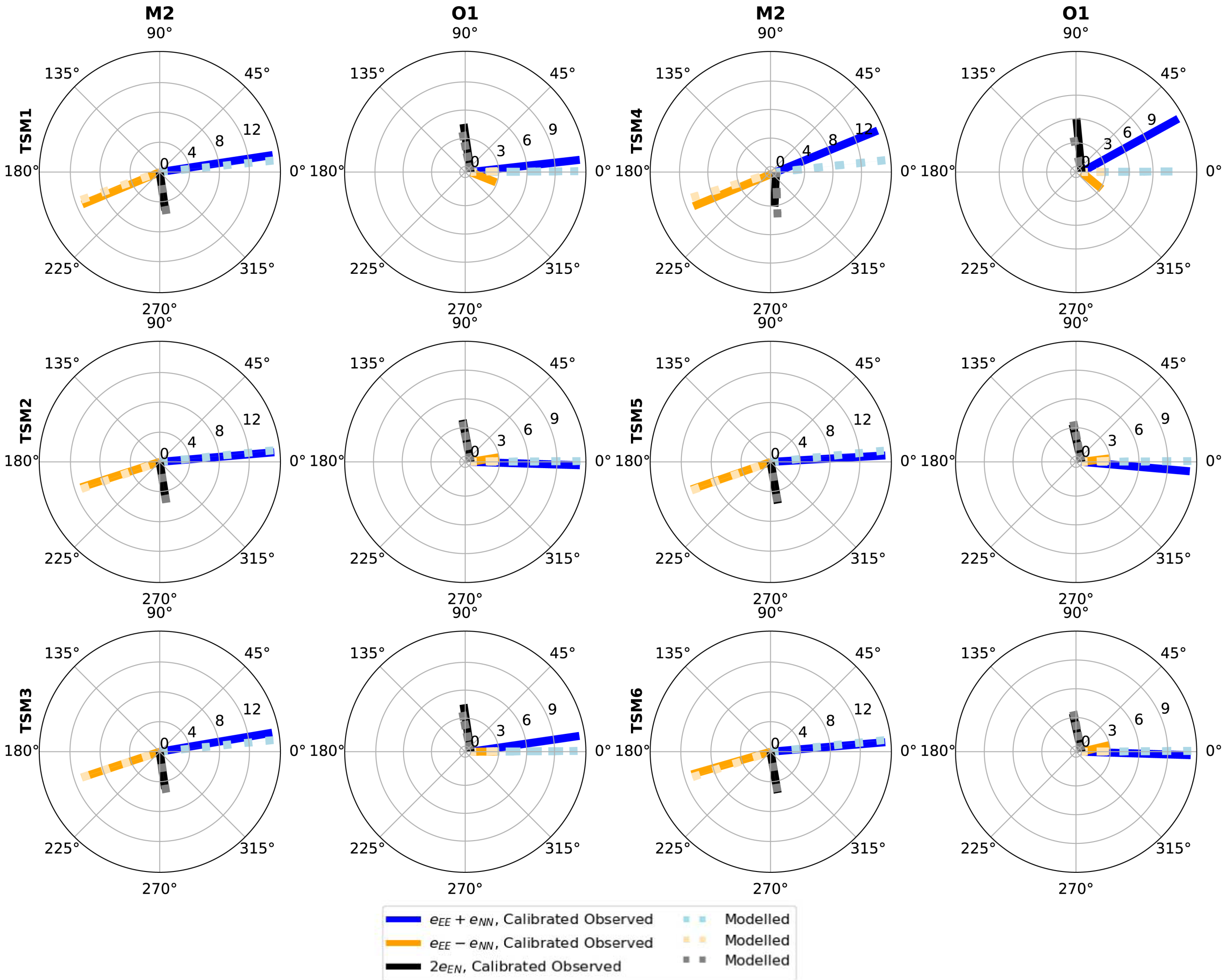

Figure 4 Polar plots showing the tidal calibration results. The observed M2 and O1 tides have been transformed with the tidal calibrations, and plotted with the SPOTL predicted tides. The concentric circles delineate amplitudes of the tidal constituents in nanostrain, while the angles of the converging lines denote the phase in degrees. Note the figure legend below for colors and line styles.

range -1 < c < 4, and 0.1 < d < 5 (Hodgkinson et al., 2013). Table S7 contains the calculated coefficients, showing none of the sites have calculated shear coefficients that wholly satisfy this criterion, though all sites have plausible areal coupling coefficients. As commonly noted with the NOTA instruments (Hodgkinson et al., 2013; Roeloffs, 2010), the STAR instruments exhibit negative areal coupling coefficients for at least one gauge. Given that the areal coefficients are plausible while the shear coefficients, which depend on the gauge orientations, are not, we infer that the orientations recorded at the time of installation could be inaccurate. However, based on the coupling coefficients alone, we cannot discount the possibility that the tidal calibrations are also in error, with either biased tidal estimates or misrepresentative modeled tidal strains contributing to the anomalous coupling coefficient values. The later analyses of coseismic earthquake strains (Sections 3.3 and 3.4) help to verify that the modeled tidal strains seem adequate for calibration.

An alternative, though similar, approach to tidal calibration from Mandler et al. (2024) is described in Supplemental Text B with associated orientation matrices in Table S8. One main difference with these calibrations is that they convert directly from counts to strain, and therefore skip the linearization process. The results are similar to the tidal calibrations presented here in the main text, as demonstrated through a timeseries comparison in Figure S5, and a map view comparison of the static offsets recorded following the Mw 5.5 Ancona event in Figure S6.

3.2 Response to surface loads

As mentioned in the previous section, the overall areal coupling of the strainmeters is negative for four of the six sites, which could indicate a high degree of coupling to vertical strain that reverses the tidally calibrated areal strain response to tectonic signals and surface loads (Roeloffs, 2010). We describe the strain response to two

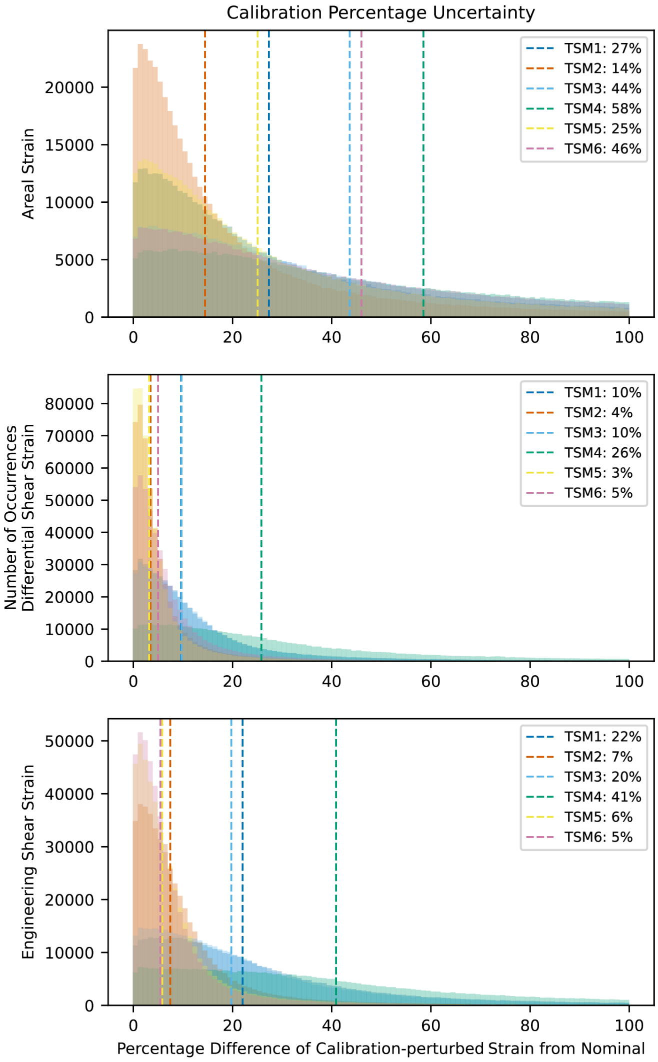

Figure 5 Uncertainty results for each station's tidally calibrated regional strain components, calculated from 500 plausible gauge strain combinations and 1000 perturbed calibration matrices given the model covariance from the tidal inversion (described in Section 2.1). The histograms contain the percentage difference of the perturbed strain values from the nominal strain values, and are color-coded by station to match the legend. The 1-standard deviation trimmed mean percentage difference is marked with a vertical dashed line for each station, and listed in the legend, corresponding to the values presented in Table 1. This percentage represents the uncertainty on the tidally calibrated regional strains.

types of surface loads to demonstrate the effect: rainfall and atmospheric pressure. Taking atmospheric pressure as an example, individual gauges contract in response to pressure increase (Figure 3). Likewise, the manufacturer's calibrated areal strain response to atmospheric pressure increase is contractional (Figures 6 and S7). For TSM1 and 2, with positive overall areal coupling, the tidally calibrated areal strain response follows the same pattern (Figures 6 and S7). The tidally calibrated areal strains at TSM3-6, however, are flipped, with an extensional response to increased atmospheric pressure (Figures 6 and S7). Rainfall invokes a similar response at the stations (Figures 6 and S8), with tidally calibrated strains that result in rapid compression at TSM1 and 2 for increased water loads, but extension at TSM3 through 6 for the same signal. However, we note that the response to rainfall could be more complex than stated here depending on the hydrologic conditions surrounding the borehole, and use it as an additional data point with cautious interpretation (e.g. Wolfe et al., 1981).

As observed for the NOTA strainmeters (Hodgkinson et al., 2013; Roeloffs, 2010), the STAR sites with primarily negative areal coupling also exhibit large magnitude barometric pressure responses (> 5 nanostrain/hPa). At TSM3 through 6, at least two gauges have barometric pressure response magnitudes > 5 nanostrain/hPa (Figure S9), with the largest response recorded at TSM4. Overall, the tidal calibrations are necessary to better represent tectonic formation strains because of this effect. However, they misrepresent strains from surface loads at TSM3 through TSM6. This adds an additional level of complexity for tectonic interpretations if a change in water level coincides with a signal of interest.

3.3 Dynamic strain results

The low-frequency longitudinal body waves recorded at TSM1, 2, 3, 5, and 6 from the Mw 5.5 Ancona and Mw 7.8 Kahramanmaras earthquakes show consistent alignment with the back-azimuths of the events (Figure 7; Table S9).

The low-frequency manifestation of the Ancona P wave arrival, as expected from the moment tensor radiation pattern, is extensional. Apparent velocities calculated from the earthquake start time to the time of peak extension range from 4.1 to 4.4 km/s, suggesting a direct, upgoing takeoff angle consistent with slow near-surface velocities traveling through basin sediments, plus a few second delay between the ambiguous wave onset and time to peak extension. For reference, the apparent velocities from the IASP91 travel times approach 5.8 km/s for the P wave (Kennett and Engdahl, 1991). The filtered amplitudes range from 67 to 112 nanostrain. Figure S2 overlays the high-frequency and filtered time series for TSM1. TSM1 and TSM6 have magnitudes exceeding the other stations by 20 nanostrain, but agree well in direction (Figure 7; Table S9). Angular misfits between the extensional strain axis and the azimuth of the event vary between 4 and 9 degrees (Figure 7; Table S9).

Both the low-frequency P and PP waves for the Kahramanmaras earthquake exhibit contractional maximum principal strain, consistent with the event radiation pattern. The apparent velocities from the start of the event to the time of peak compression for the P and PP arrivals are ~7.9 and 7.4 km/s for the respective phases, consistent with significant travel through the mantle. This is again delayed from the IASP91 estimated apparent velocities of 8.1 and 7.7 km/s, though the greater event distance diminishes the path differences from the global velocity model estimates. Amplitudes of the filtered P wave compressional axis range from -0.7 to -1.6 nanostrain, though the relatively large high-frequency over-

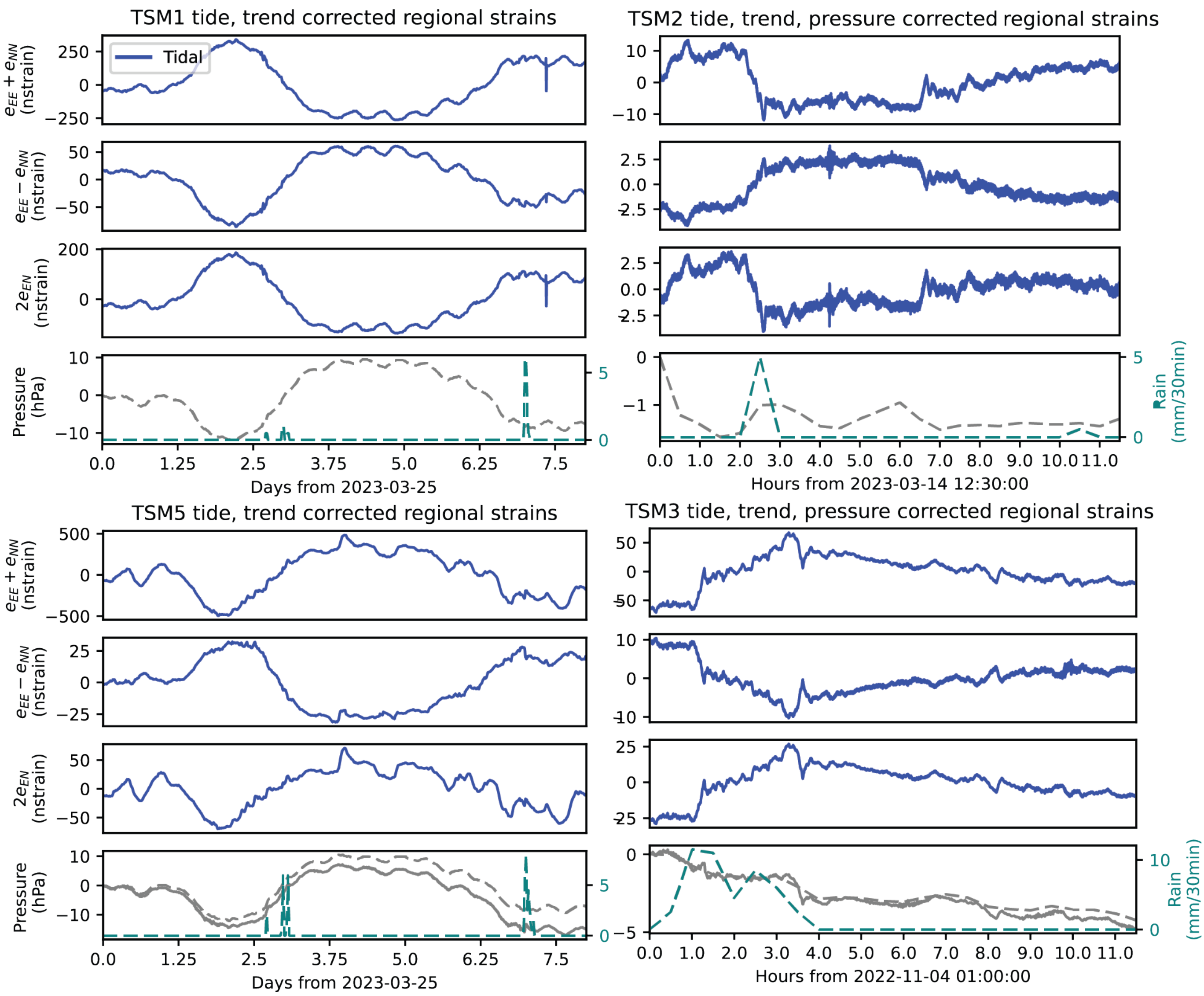

Figure 6 Comparison of regionally transformed areal (e_{EE}+e_{NN}), differential (e_{EE}-e_{NN}), and shear ($2e_{EN}$) strain time series using the tidal calibrations. Barometric pressure (dashed grey) and rainfall intensity (dashed teal) are plotted for comparison, with pore pressure at TSM3 and TSM5 (solid grey). Note the secondary y-axis for rainfall. The left plots show response to barometric pressure changes over the course of a week, while the right plots show a response to rainfall for a half-day. The time series have been zeroed to the first value. TSM3 and 5 exhibit negative areal coupling, with dilation (positive) in response to pressure increase.

print makes precise calculation uncertain (Table S9). The average magnitude of the PP wave compressional axis is larger, ranging from -23.0 to -27.1 nanostrain. Angular misfit to the event azimuth ranges from <1 to 12 degrees (Figure 7; Table S9).

3.4 Static strain results

Following the passage of the dynamic earthquake body wave strains, coseismic static strain offsets are observed at each station for the Ancona and Kahramanmaras earthquakes, in addition to the local Umbertide foreshock and mainshock. The static strain results, presented in Figure 8 and Table S11, show a greater variability between the expected and observed strains than for the dynamic signals, as well as a greater interstation amplitude variability, but demonstrate quite consistent orientations with each modeled event.

The coseismic static strain amplitude misfit is variable for the near field earthquakes and underpredicted for the far field earthquakes (Figure 8; Table S11). For the near field Umbertide sequence, TSM1 matches the magnitude of the Mw 4.3 event within half of a nanostrain, but has larger observed than modeled strain for the Mw4.5 event. For TSM2, modeled strain magnitudes slightly over and underpredict the Mw 4.3 and 4.5 observed static strains, respectively. TSM6 matches well with strain magnitudes for the near field events, approaching single- to sub-nanostrain offsets (Table S11). TSM3 fails to match any event well in magnitude or direction. While the observed amplitudes are on the same order of magnitude as the modeled amplitudes for the near-field events, ranging from single to 10s of nanostrain, the modeled magnitudes for the Ancona event are an order of magnitude larger than the sub-nanostrain offsets expected. Figure 7 modeled coseismic offsets for the Mw 7.8 Kahramanmaras event are amplified by 20

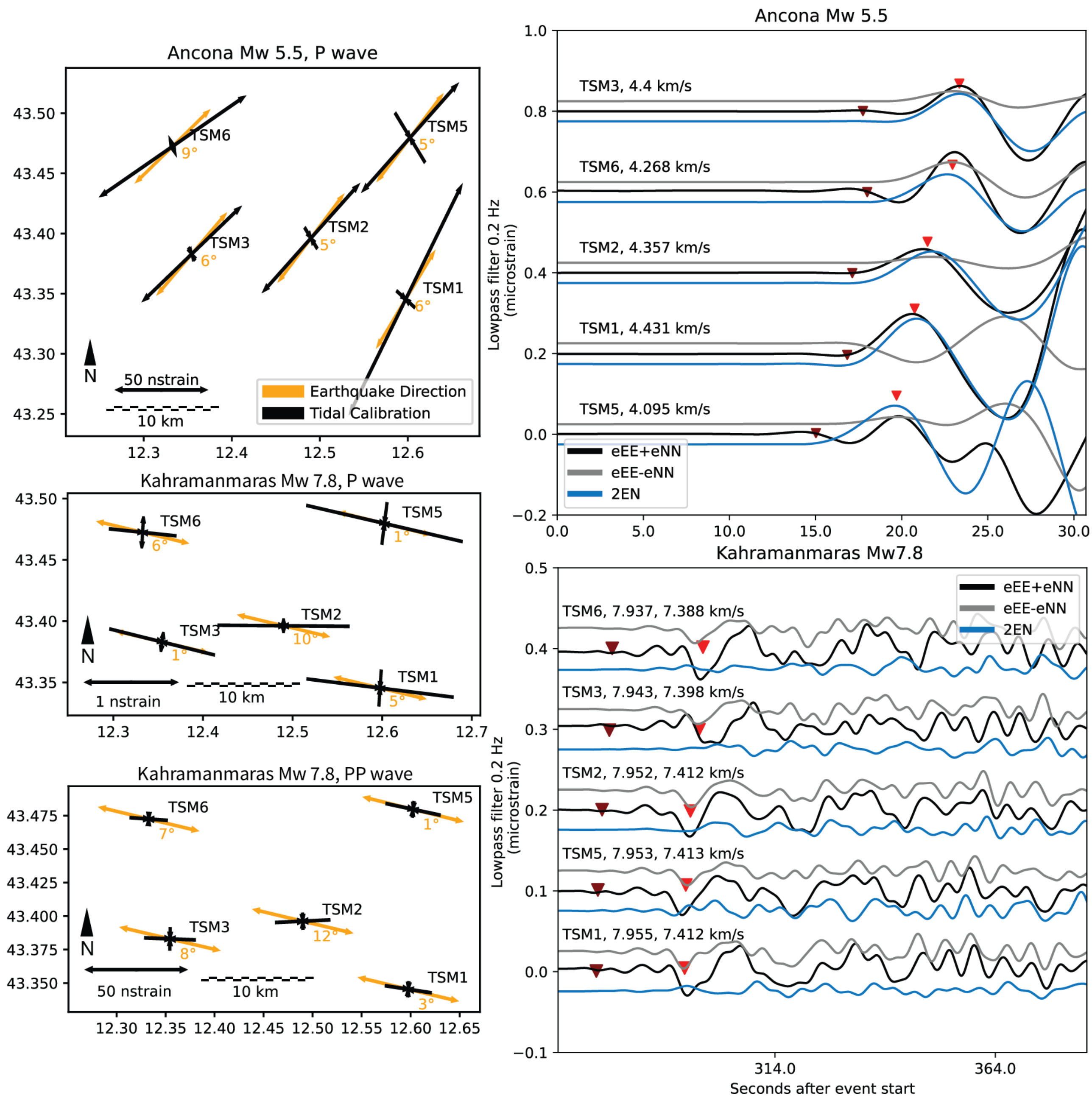

Figure 7 (Top right) Tidally calibrated and filtered dynamic strains for the Mw 5.5 Ancona low-frequency P wave at all stations, in order of distance from the event epicenter from bottom to top. The first triangle on each time series marks the P arrival from the collocated borehole seismometers. The second triangle marks the time of peak extensional strain associated with the low-frequency signal, and the apparent velocity for each station to the time of the peak extension is printed. The corresponding axis of maximum extension is pictured in the (top left) maps, with the black arrows scaled to the magnitudes of maximum and minimum principal strain, and the orange directional arrow aligned to the event azimuth. The directional misfit between the maximum horizontal strain axis and azimuth of the event is labeled in degrees. Similar (bottom right) plots are presented for the Mw 7.8 Kahramanmaras earthquake, but the first and second triangles on the time series in the (bottom right) plot mark the peak compressional P and PP waves with the calculated velocities.

times the nominal values to visualize the strains with the observed coseismic offsets, demonstrating a significant underprediction of coseismic strain magnitudes for the far field events (Table S11). Furthermore, the predicted strains for both far field events are quite consistent between stations, while the observations again vary by an order of magnitude.

While the strain magnitudes show variable agreement between the observations and model, the orientations match well. The largest discrepancies (>15°) occur at TSM6 for the Mw 7.8 Kahramanmaras and Mw 4.3 Umbertide earthquakes. The angular misfits for the Umbertide earthquakes are sensitive to the strike and rake of the rupture parameters given its close proximity to the instruments, as demonstrated through initial tests of various strikes and rakes within the uncertainty bounds of the focal mechanism solution.

4 Discussion

The tidally calibrated STAR instruments show useful and interpretable results for earthquake deformation signals originating from immediate to 1000s of kilometer distances, expanding the capabilities of the existing geophysical and geochemical network in the Alto Tiberina Near Fault Observatory (Figure 1; Chiaraluce et al., 2014, 2024). We continue our discussion of the tidal calibration results for various reference signals, highlighting which assumptions of the manufacturer's calibrations fail to capture the complexity of these stations. Then, we characterize the stations' responses in the context of previous borehole strain observations, with particular focus on TSM3 as a demonstration of influence from several unexpected but interpretable environmental and earthquake-related signals, which may help to guide future analyses of strains recorded at these sites and elsewhere globally.

The failure of the manufacturer's calibrations to capture the in situ strain field at the STAR sites reveals details of the installation conditions. First, failed gauge consistency checks imply directional variability in the layered, gently to moderately dipping strata of the installation zones, and/or differences in each gauge's instrumental gain, known to vary by as much as 20% (Figure S4; Roeloffs, 2010). Second, calculation of physically unreasonable shear coupling coefficients from the tidal calibrations and reported installation orientations indicate error in the latter, as noted for many NOTA BSMs (e.g. Hodgkinson et al., 2013). Third, relatively larger tidally versus manufacturer's calibrated strains implies a higher grout-to-formation strength ratio than assumed for the manufacturer's calibrations (Gladwin and Hart, 1985). This is unsurprising given the site host lithologies of fractured sandstones, marls, and limestones, as opposed to the intact granite-like strengths assumed for the manufacturer's calibrations (Chiaraluce et al., 2024; Hodgkinson et al., 2013; Attewell and Farmer, 1976). Finally, and most importantly, the manufacturer's calibrations cannot account for negative areal coupling in four (TSM3-6) of the six strainmeters. This may result from non-negligible response to the vertical strain field (Roeloffs, 2010), making the tidal calibrations critical for characterizing the areal strain response to tectonic events. The response to surface loads, however, is not valid with the tidal calibrations, as also alluded to in Roeloffs (2010). Overall, these results indicate that the non-constrained solutions of the tidal calibrations are critical for analyzing tectonic deformation with the STAR BSM data.

In line with this recognition, the tidal calibrations show remarkable success for resolving dynamic and static strain orientations for signals on the order of a few nano-strain. This is reflected by the relatively lower uncertainty of the regional shear strains than the areal strains, because the shears primarily constrain the principal strain directions (Figure 5; Table 1). There are a few station-specific exceptions showing misfit >15° with respect to the expected principal strain directions (Figures 7 and 8; Tables S8 and S11). For example, the observed static strains for TSM6 from the Mw 7.8 Kahramanmaras event are misoriented by 22°, but uncorrected response from environmental influences could easily bias the small (<3 nanostrain) offsets in addition to the 5% shear strain uncertainty from the calibrations (Table 1). The pore pressure transducer was not recording during the event, so we have no indication of whether high-rate barometric or hydrologic changes could have influenced the station. The largest static directional misfit for the network occurred from the near field Umbertide Mw 4.5 earthquake. However, more appropriate fit between the modeled and observed strains is within both the calibration uncertainty as well as the earthquake parameter uncertainties, including the location, strike, dip, and rake of the event. Furthermore, the lack of systematic orientation discrepancy between the stations, or for the same station between different events, may indicate random variability as expected for any real-world signal and data. We note that static coseismic offset magnitudes for similar instruments elsewhere are estimated to be unreliable most of the time, independent of distance from the earthquake (~90%; Barbour, 2015); However, our findings indicate this may result more from amplitude errors than orientation discrepancies if proper calibrations are realized.

Significantly inflated observed static strain amplitudes relative to the modeled strain requires further global context, and, while not uncommon, remain an outstanding unexplained phenomenon (Figure 8). The first clear pattern is an underestimation of model magnitudes for the Ancona and Kahramanmaras earthquakes, with misfit that increases with distance beyond the estimated calibration uncertainty (Figure 8; Table S11). The observed static strain offsets for both the Ancona and Kahramanmaras events reveal comparable magnitudes despite that they should differ by an order of magnitude (Table S11). Furthermore, the Kahramanmaras offsets should barely be detectable amidst the high- magnitude and frequency dynamic strain signal. Although we use a simple elastic half-space approximation to estimate offsets, the effects of Earth's curvature and elastic structure should further diminish, not increase, the strain response (Guangyu et al., 2011; Sun et al., 2009; Pollitz, 1996). This observation of inflated areal or volumetric static strains is common (Wang and Barbour, 2017). Several candidate mechanisms are invoked to explain this far field effect, including local heterogeneities or topographic influence (Beaumont and Berger, 1975), microcrack yielding (Barbour, 2015), local changes in groundwater level (Zhang et al., 2016), and pore pressure response local to the borehole, demonstrated as potentially dominant from far field sources for distances out to ~5500 km (Wang and Barbour, 2017). We expect the tidal calibrations to correct for topographic effects, but these other mechanisms could bias amplitude estimates while preserving overall strain orientation.

In contrast, the static strain amplitudes appear valid within the array footprint, as demonstrated for the near field Umbertide sequence (Figure 8). The small magnitude strains at TSM6 (< 2 nanostrain) show a capabil-

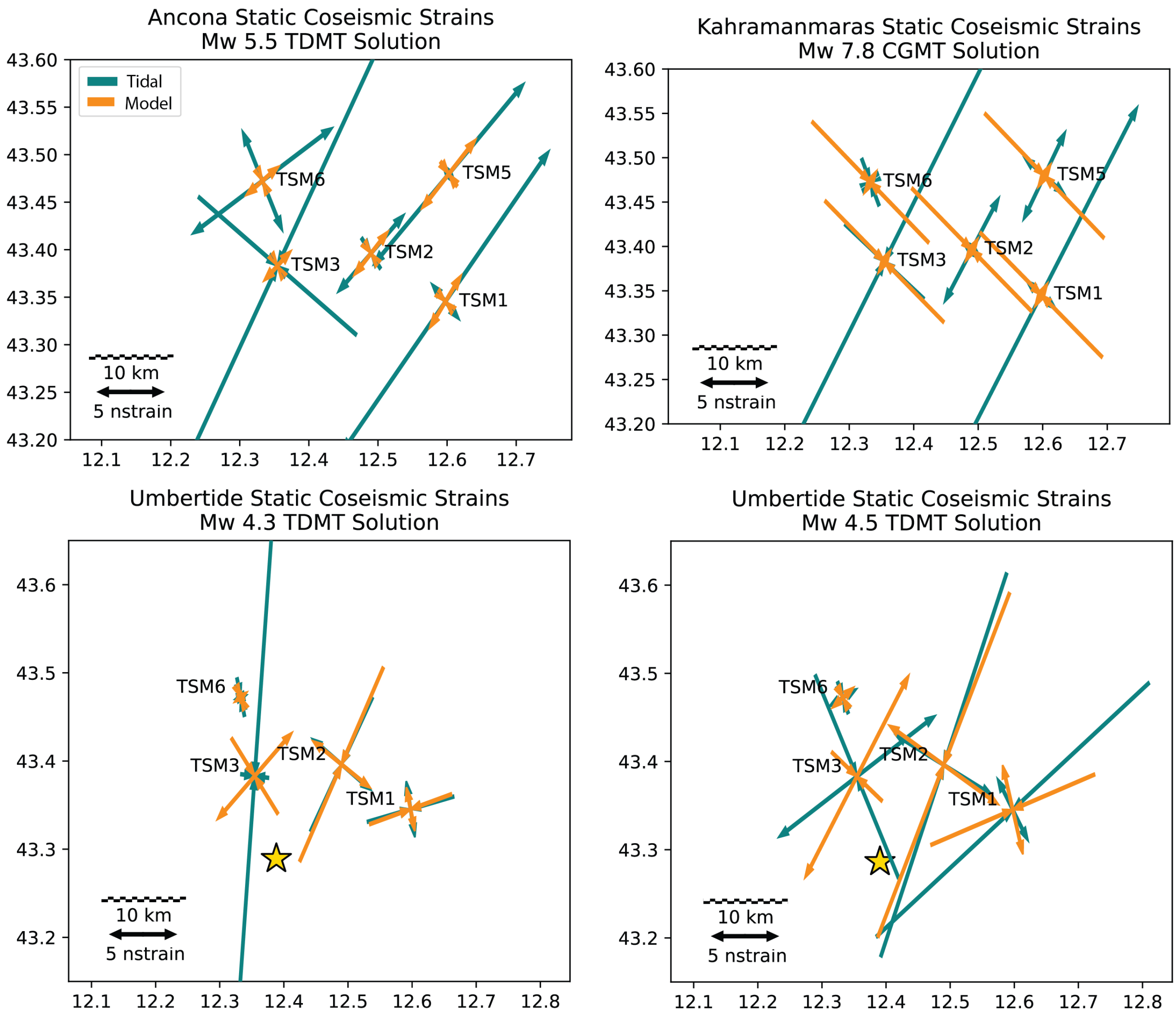

Figure 8 Coseismic strains transformed with the tidal calibrations compared with the modeled strains for each earthquake in map view. For the Umbertide events, the yellow stars mark the Mw 4.3 and 4.5 events, which occurred at depths of 3 and 3.3 km, respectively. Differences in the coseismic strain, despite nearly collocated events, demonstrate a high level of instrument sensitivity with some calibration uncertainty. For the Kahramanmaras event, the modeled strains have been amplified by 20 times the nominal values to allow a visual comparison of the principal strain axis directions. The strain axes have been clipped by the map frame for viewing purposes, and we refer the reader to Table S11 for the strain amplitudes at TSM3, but note that the maximum principal strain axis is compressional at the station for all events.

ity for capturing minute deformation, despite the nominally higher percentage uncertainties estimated for the calibration (Figure 5; Table 1). This achievement for both events suggests that the inability to capture far field strain amplitudes is less of an issue for events within the array footprint. While further quantitative characterization of offset uncertainty is not possible with such a small dataset, the lack of systematic over- or under- estimation of near field strain amplitudes for any single station supports the validity of the tidal models for calibration within the inversion uncertainty (Figure 5; Table1). This holds despite the findings of Langbein (2010, 2015), which estimate a potential 10-30% uncertainty from the tidal calibrations considering the lack of precision and accuracy of the tidal models. We demonstrate that similar uncertainty may result from the inversion without considering tidal model errors; although, for these stations, the uncertainty demonstrably does not prevent the retrieval of useful, calibrated data, especially if considering correspondence within the whole network. Thus, the calibrated stains are a useful addition to the existing TABOO-NFO geophysical network.

TSM3 recorded static strain offsets that far exceed those of the other stations, even for the near-field events. We attribute this to possible borehole-local fracture slip with enhanced permeability and fluid flow

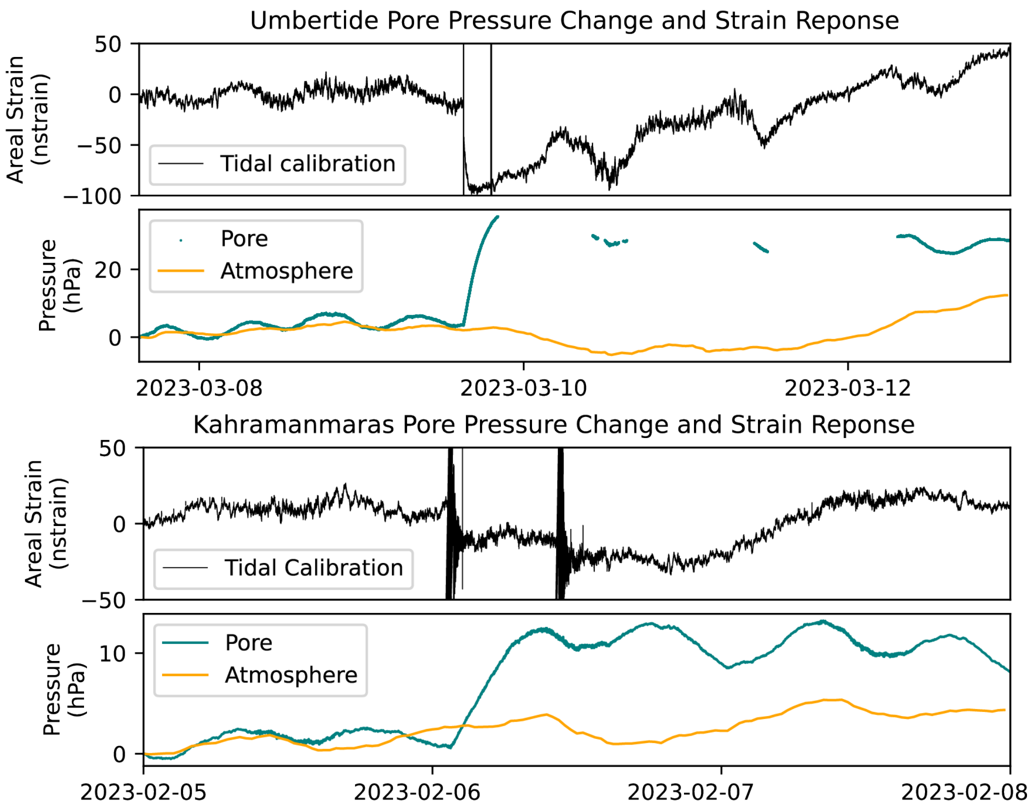

Figure 9 TSM3 areal strain response to the Mw 5.5 Ancona and Mw 7.8 Kahramanmaras earthquakes plotted with the pore pressure transducer response for the same time interval. The colors for each dataset appear in the legends. Large gaps are present in the pore pressure record for the Umbertide events. In both cases, pore pressure changes are observed prior to the second large magnitude event of the sequence.

through a series of observations. First, TSM3 experiences large magnitude compressional static strain offsets that are similarly misoriented (to the N-NE) for the far field earthquakes. This does not, however, mean that the calibrations are in error, because the station behaves as expected in response to dynamic strains from the longitudinal body waves (Figures 7 and 8). Second, discrepancies in the static strains at TSM3 are accompanied by borehole-local water level readjustments (Figure 9 and S10). Local changes in water level have been observed from earthquakes at teleseismic and near distances, attributed, respectively, to (1) dynamically enhanced permeability that permits fluid flow (e.g. Elkhoury et al., 2006; Zhang et al., 2016), and/or (2) postseismic poroelastic relaxation as water flows in response to relatively large magnitude volumetric strain changes that perturb pore fluid pressures at a regional scale (Peltzer et al., 1998; Segall et al., 2003). We hypothesize that both may have occurred at TSM3, with potential dynamic enhancement of permeability that permitted fluid flow and diminished the frictional resistance of a local fracture (e.g. Cocco and Rice, 2002), enabling slip in response to large magnitude dynamic strains with a preferential N-NE oriented compressional signature.

Coseismically, for three of the four earthquakes we observe changes in water level that support the first hypothesis of dynamically enhanced permeability with fracture slip at TSM3. We did not observe a change in water level following the Ancona earthquake, despite that the observed compressional strains are consistent with the hypothesis (Figure 8). However, the hydraulic connection of the borehole at the level of the pore pressure sensor may not have been established until sometime following the Ancona event, supported by the observation that the pore pressure sensor primarily tracked barometric pressure changes with no response to rainfall 5 days before the Ancona earthquake, indicating no connection to surrounding water level changes (Figure 6). In contrast, pore pressure tracks the tides for the later earthquakes, indicating new flow of water into the borehole (Figure 9; Figure S10). The borehole was mud-caked at the time of installation, so it is possible that this mud initially blocked water flow, and was subsequently dislodged. For the local Mw 4.3 event, the static strain offsets rotate toward the expected static strain field, and nearly agree with the modeled strains for the Mw 4.5 event, showing that the local strain overprint from fracture slip can be biased toward the larger near field earthquake strains (Figure 7).

Postseismically, we observe the second effect of potential poroelastic influence on strains at TSM3. The station experienced a pronounced postseismic areal compression following the Umbertide sequence (Figure 9). The borehole-local perturbation to water level from fracture-guided fluid flow may have been accompanied by more regional-scale readjustment of water levels following the coseismic volumetric compression imposed by the earthquakes. Correspondingly, postseismic areal contraction (actual gauge extension due to the negatively coupled response to areal strain from the tidal calibrations) experienced at TSM3 may mark the poroelastic transition from the undrained to drained state as water flows away from the instrument (Peltzer et al., 1998; Segall et al., 2003). Detection of this potential regional water level adjustment could aid in future studies of poroelastic deformation, which has so far been limited by the lower resolution of GNSS (e.g. Nespoli et al., 2018). Overall, TSM3 appears to have a valid tidal calibration, but anomalous instrument and pore pressure response following large magnitude seismic waves prompts caution for analyzing deformation during and following high strain rate events. Likewise, the pore pressure transducer does not always track rock formation pore pressures. This could complicate the combined interpretation of pore pressure and strain data – postseismic deformation at the BSM may be of tectonic or hydrologic origin, regardless of what is recorded at the pore pressure transducer.

Future study could tighten the uncertainty bounds on the calibrated strain amplitudes, afforded through a comparison with alternative measurements from, for example, an array of collocated seismometers (Currenti et al., 2017). TSM4 would benefit most from an alternative calibration strategy, because the strong negative areal coupling response indicated by large barometric pressure-induced fluctuations (Figure S10; Table S3), low tidal power (Figure S4; Table S5), and relatively large calibration misfit and uncertainty (Figure 5; Table 1 and S5) indicate further testing is critical to determine whether the tidal calibrations are useful. As longer, cleaner time series with diminished borehole relaxation trends become available, TSM4 and the other STAR site calibrations can be re-evaluated. In the meantime, accurate detection of emergent strains from aseismic slip, absent of potential complications that arise from high magnitude and frequency dynamic strains, is enhanced by the tidal calibrations. All modeled displacement estimates at the distances analyzed in this study fall below the detection thresholds of conventional GNSS or InSAR observations (sub-mm); therefore, the presence of the calibrated STAR array complements and enhances the network in its goal for detecting slip on the ATF and its surrounding active structures.

5 Conclusion

The tidally calibrated STAR BSM instruments expand the geophysical network capabilities of the Alto Tiberina Near Fault Observatory (Figure 1; Chiaraluce et al., 2014). The manufacturer's calibrations assumptions of isotropic, homogeneous rock conditions with equal coupling on all gauges and presumed effective moduli fail to capture the complex STAR BSM response. The tidally calibrated network demonstrates remarkable precision for resolving orientations of signals approaching nanostrain levels, as observed for the directionally polarized low-frequency P and PP body waves from the 90 km and 2000 km distant Mw 5.5 Ancona and Mw 7.8 Kahramanmaras earthquakes. Similarly, near field (10s km) coseismic strains for the Umbertide Mw 4.3 and 4.5 events may indicate a high sensitivity to source parameters, showing no consistent over- or under- estimation suggestive of poor tidal model accuracy given that the results remain within the calibration inversion uncertainty. The far field static strain amplitudes exhibit discrepancies consistent with other studies (e.g. Wang and Barbour, 2017), though with previously unnoted angular agreement. Improvement on these tidal calibrations could be afforded by a reanalysis as longer, cleaner time series become available, and/or through comparison with independent surface measurements of strain (e.g. Currenti et al., 2017), particularly at TSM4 where station outages prevented much of the testing carried out here. TSM3 exhibits anomalous behavior potentially associated with dynamically triggered near field fracture slip and fluid flow, but without sacrificing sensitivity to deformation at lower strain rates. Four of the six STAR BSMs (TSM3-6) are negatively coupled to areal strain, which makes the tidal calibrations invalid for accurately studying deformation related to widely distributed surface loads. Nonetheless, with cautious interpretation, the combination of areal gauge strain and pore pressure change can provide insight for low strain-rate processes, such as the potential poroelastic relaxation experienced at TSM3 following the Umbertide earthquake sequence. Importantly, all deformation analyzed in this study falls below the detection threshold of more conventional geodetic techniques, leaving promise for future STAR potential in detecting spatiotemporally variable aseismic slip associated with the ATF and overlying active faults.

Acknowledgements

This work was initially supported by the NSF grant 1723045 to the University of Arizona, scholarships awarded through the University of Arizona Department of Geosciences (the Sulzer and Sumner Scholarships), and further supported through NASA grant 21-DSI-21-0003 and the National Earthquake Hazard Reduction Program. The STAR project was partly supported by the International Continental Scientific Drilling Program (ICDP; https://www.icdp-online.org/projects/by-continent/europe/star-italy) in addition to the institutions represented in the author list. We would like to thank two anonymous reviewers for their feedback that improved the clarity and quality of the manuscript.

Data and code Availability

No new data was collected for the purpose of this study. All raw data is available as indicated in the main text of here. The processing and calibration workflow presented here is now implemented in the Earthscopestraintools python package (Gottlieb and Hanagan, 2024, https://earthscopestraintools.readthedocs.io/en/latest/index.html), along with the preferred tidal calibrations available through the package and in the station metadata read me files (e.g. http://bsm.unavco.org/bsm/level2/tstartsm2bit2021/TSM2.README.txt). Instrumentally recorded and historical earthquakes of interest for the TABOO NFO (FDSN-event), and TABOO CO2, seismic, and GNSS site locations are provided through INGV - Istituto Nazionale di Geofisica e Vulcanologia,

https://creativecommons.org/licenses/by-nc/4.0/, last accessed on 30-07-2024 through the EPOS Data Portal (https://www.epos-eu.org/dataportal). The facilities of IRIS Data Services, and specifically the IRIS Data Management Center, were used for access to waveforms, related metadata, and/or derived products used in this study. Specifically, the raw borehole strain data are managed by EarthScope (UNAVCO) as part of the NOTA Borehole Seismic Network, available through web services (https://service.iris.edu/fdsnws/). IRIS Data Services are funded through the Seismological Facilities for the Advancement of Geoscience (SAGE) Award of the National Science Foundation under Cooperative Support Agreement EAR-1851048. Any use of trade, firm, or product names is for descriptive purposes only and does not imply endorsement by the U.S. Government. Many figures were prepared with the GMT software (Wessel et al., 2019) or the Python Matplotlib package (Hunter, 2007). All other software used is available as designated in the original publications.

Competing Interests

The authors have no competing interests.

References

Agnew, D. SPOTL: Some Programs for Ocean-Tide Loading, 2012. https://escholarship.org/uc/item/954322pg. Retrieved from.

Amoruso, A. and Crescentini, L. The geodetic laser interferometers at Gran Sasso, Italy: Recent modifications and correction for local effects. *Journal of Geodynamics*, 48(3–5):120–125, 2009. doi: 10.1016/j.jog.2009.09.025.

Anderlini, L., Serpelloni, E., and Belardinelli, M. E. Creep and locking of a low-angle normal fault: Insights from the Altotiberina fault in the Northern Apennines (Italy). *Geophysical Research Letters*, 43(9):4321–4329, 2016. doi: 10.1002/2016gl068604.

Attewell, P. B. and Farmer, I. W. *Principles of Engineering Geology*. Springer Netherlands, 1976. doi: 10.1007/978-94-009-5707-7.

Bailo, D., Paciello, R., Michalek, J., Cocco, M., Freda, C., Jeffery, K., and Atakan, K. The EPOS multi-disciplinary Data Portal for integrated access to solid Earth science datasets. *Scientific Data*, 10 (1), 2023. doi: 10.1038/s41597-023-02697-9.

Barbour, A. J. Pore pressure sensitivities to dynamic strains: Observations in active tectonic regions. *Journal of Geophysical Research: Solid Earth*, 120(8):5863–5883, 2015. doi: 10.1002/2015jb012201.

Barbour, A. J., Agnew, D. C., and Wyatt, F. K. Coseismic Strains on Plate Boundary Observatory Borehole Strainmeters in Southern California. *Bulletin of the Seismological Society of America*, 105 (1):431–444, 2014. doi: 10.1785/0120140199.

Beaumont, C. and Berger, J. An analysis of tidal strain observations from the United States of America: I. The laterally homogeneous tide. *Bulletin of the Seismological Society of America*, 65(6):1613–1629, 1975. doi: 10.1785/bssa0650061613.

Canitano, A., Bernard, P., Linde, A. T., Sacks, S., and Boudin, F. Correcting High-Resolution Borehole Strainmeter Data from Complex External Influences and Partial-Solid Coupling: the Case of Trizonia, Rift of Corinth (Greece). *Pure and Applied Geophysics*, 171(8):1759–1790, 2013. doi: 10.1007/s00024-013-0742-2.

Canitano, A., Hsu, Y.-J., Lee, H.-M., Linde, A. T., and Sacks, S. Calibration for the shear strain of 3-component borehole strainmeters in eastern Taiwan through Earth and ocean tidal waveform modeling. *Journal of Geodesy*, 92(3):223–240, 2017. doi: 10.1007/s00190-017-1056-4.

Chiaraluce, L., Chiarabba, C., Collettini, C., Piccinini, D., and Cocco, M. Architecture and mechanics of an active low-angle normal fault: Alto Tiberina Fault, northern Apennines, Italy. *Journal of Geophysical Research: Solid Earth*, 112(B10), 2007. doi: 10.1029/2007jb005015.

Chiaraluce, L., Amato, A., Carannante, S., Castelli, V., Cattaneo, M., Cocco, M., Collettini, C., D'Alema, E., Stefano, R. D., Latorre, D., Marzorati, S., Mirabella, F., Monachesi, G., Piccinini, D., Nardi, A., Piersanti, A., Stramondo, S., and Valoroso, L. The Alto Tiberina Near Fault Observatory (northern Apennines, Italy). *Annals of Geophysics*, 57(3), 2014. doi: 10.4401/ag-6426.

Chiaraluce, L., Bennett, R., Mencin, D., Johnson, W., Barchi, M. R., Bohnhoff, M., Baccheschi, P., Caracausi, A., Calamita, C., Cavaliere, A., Gualandi, A., Mandler, E., Mariucci, M. T., Martelli, L., Marzorati, S., Montone, P., Pantaleo, D., Pucci, S., Serpelloni, E., Supino, M., Stramondo, S., Hanagan, C., Van Boskirk, L., Gottlieb, M., Mattioli, G., Urbani, M., Mirabella, F., Akimbekova, A., Pierdominici, S., Wiersberg, T., Marone, C., Palmieri, L., and Schenato, L. A strainmeter array as the fulcrum of novel observatory sites along the Alto Tiberina Near Fault Observatory. *Scientific Drilling*, 33(2):173–190, 2024. doi: 10.5194/sd-33-173-2024.

Cocco, M. and Rice, J. R. Pore pressure and poroelasticity effects in Coulomb stress analysis of earthquake interactions. *Journal of Geophysical Research: Solid Earth*, 107(B2), 2002. doi: 10.1029/2000jb000138.

Currenti, G., Zuccarello, L., Bonaccorso, A., and Sicali, A. Borehole Volumetric Strainmeter Calibration From a Nearby Seismic Broadband Array at Etna Volcano. *Journal of Geophysical Research: Solid Earth*, 122(10):7729–7738, 2017. doi: 10.1002/2017jb014663.

Dziewonski, A. M., Chou, T., and Woodhouse, J. H. Determination of earthquake source parameters from waveform data for studies of global and regional seismicity. *Journal of Geophysical Research: Solid Earth*, 86(B4):2825–2852, 1981. doi: 10.1029/jb086ib04p02825.

Egbert, G. D. and Erofeeva, S. Y. Efficient Inverse Modeling of Barotropic Ocean Tides. *Journal of Atmospheric and Oceanic Technology*, 19(2):183–204, 2002. doi: 10.1175/1520-0426(2002)019<0183:eimobo>2.0.co;2.

Ekström, G., Nettles, M., and Dziewoński, A. The global CMT project 2004–2010: Centroid-moment tensors for 13,017 earthquakes. *Physics of the Earth and Planetary Interiors*, 200–201:1–9, 2012. doi: 10.1016/j.pepi.2012.04.002.

Elkhoury, J. E., Brodsky, E. E., and Agnew, D. C. Seismic waves increase permeability. *Nature*, 441(7097):1135–1138, 2006. doi: 10.1038/nature04798.

Farr, T. The Shuttle Radar Topography Mission. *Rev. Geophys*, 45: 2004, 2007.

Farrell, W. A discussion on the measurement and interpretation of changes of strain in the Earth-Earth tides, ocean tides and tidal loading. *Philosophical Transactions of the Royal Society of London. Series A, Mathematical and Physical Sciences*, 274(1239): 253–259, 1973. doi: 10.1098/rsta.1973.0050.

Farrell, W. E. Deformation of the Earth by surface loads. *Reviews of Geophysics*, 10(3):761–797, 1972. doi: 10.1029/rg010i003p00761.

Gladwin, M. T. High-precision multicomponent borehole deformation monitoring. *Review of Scientific Instruments*, 55(12): 2011–2016, 1984. doi: 10.1063/1.1137704.

Gladwin, M. T. and Hart, R. Design parameters for borehole strain instrumentation. *pure and applied geophysics*, 123(1):59–80, 1985. doi: 10.1007/bf00877049.

Gottlieb, M. and Hanagan, C. EarthScope/earthscopestraintools: v0.1.42 (V0.1.42-beta) [software]. Zenodo, 2024. doi: 10.5281/zenodo.12193840.

Grant, E. and Langston, C. Gladwin Tensor Strain-Meter calibration and wave gradiometry applications. In *AGU Fall Meeting Abstracts*, volume 2009, page 53 –0070, 2009.

Gualandi, A., Nichele, C., Serpelloni, E., Chiaraluce, L., Anderlini, L., Latorre, D., Belardinelli, M. E., and Avouac, J. Aseismic deformation associated with an earthquake swarm in the northern Apennines (Italy). *Geophysical Research Letters*, 44(15): 7706–7714, 2017. doi: 10.1002/2017gl073687.

Guangyu, F., Xuzhang, S., Yoichi, F., Shanghua, G., and Satoshi, Y. Co-seismic strain changes of Wenchuan Mw7. 9 earthquake recorded by borehole strainmeters on Tibetan plateau. *Geodesy and Geodynamics*, 2(3):42–49, 2011. doi: 10.3724/sp.j.1246.2011.00042.

Harkrider, D. G. Surface waves in multilayered elastic media. Part II. Higher mode spectra and spectral ratios from point sources in plane layered Earth models. *Bulletin of the Seismological Society of America*, 60(6):1937–1987, 1970. doi: 10.1785/bssa0600061937.

Hart, R. H. G., Gladwin, M. T., Gwyther, R. L., Agnew, D. C., and Wyatt, F. K. Tidal calibration of borehole strain meters: Removing the effects of small-scale inhomogeneity. *Journal of Geophysical Research: Solid Earth*, 101(B11):25553–25571, 1996. doi: 10.1029/96jb02273.

Hodgkinson, K., Langbein, J., Henderson, B., Mencin, D., and Borsa, A. Tidal calibration of plate boundary observatory borehole strainmeters. *Journal of Geophysical Research: Solid Earth*, 118(1):447–458, 2013. doi: 10.1029/2012jb009651.

Hreinsdottir, S. and Bennett, R. A. Active aseismic creep on the Alto Tiberina low-angle normal fault, Italy. *Geology*, 37(8):683–686, 2009. doi: 10.1130/g30194a.1.

Hunter, J. D. Matplotlib: A 2D Graphics Environment. *Computing in Science & Engineering*, 9(3):90–95, 2007. doi: 10.1109/mcse.2007.55.

Kennett, B. L. N. and Engdahl, E. R. Traveltimes for global earthquake location and phase identification. *Geophysical Journal International*, 105(2):429–465, 1991. doi: 10.1111/j.1365-246x.1991.tb06724.x.

Langbein, J. Effect of error in theoretical Earth tide on calibration of borehole strainmeters. *Geophysical Research Letters*, 37(21), 2010. doi: 10.1029/2010gl044454.

Langbein, J. Borehole strainmeter measurements spanning the 2014 Mw6.0 South Napa Earthquake, California: The effect from instrument calibration. *Journal of Geophysical Research: Solid Earth*, 120(10):7190–7202, 2015. doi: 10.1002/2015jb012278.

Linde, A. T., Gladwin, M. T., Johnston, M. J. S., Gwyther, R. L., and Bilham, R. G. A slow earthquake sequence on the San Andreas fault. *Nature*, 383(6595):65–68, 1996. doi: 10.1038/383065a0.

Mandler, E., Canitano, A., Belardinelli, M. E., Nespoli, M., Serpelloni, E., and Linde, A. Tidal Calibration of the Gladwin Tensor Strain Monitor (GTSM) Array in Taiwan. *Pure and Applied Geophysics*, 182(3):1001–1021, 2024. doi: 10.1007/s00024-024-03453-9.

Menke, W. Review of the Generalized Least Squares Method. *Surveys in Geophysics*, 36(1):1–25, 2014. doi: 10.1007/s10712-014-9303-1.

Mirabella, F., Brozzetti, F., Lupattelli, A., and Barchi, M. R. Tectonic evolution of a low-angle extensional fault system from restored cross-sections in the Northern Apennines (Italy). *Tectonics*, 30 (6), 2011. doi: 10.1029/2011tc002890.

Nespoli, M., Belardinelli, M. E., Gualandi, A., Serpelloni, E., and Bonafede, M. Poroelasticity and Fluid Flow Modeling for the 2012 Emilia-Romagna Earthquakes: Hints from GPS and InSAR Data. *Geofluids*, 2018:1–15, 2018. doi: 10.1155/2018/4160570.

Okada, Y. Surface deformation due to shear and tensile faults in a half-space. *Bulletin of the Seismological Society of America*, 75 (4):1135–1154, 1985. doi: 10.1785/bssa0750041135.

Peltzer, G., Rosen, P., Rogez, F., and Hudnut, K. Poroelastic rebound along the Landers 1992 earthquake surface rupture. *Journal of Geophysical Research: Solid Earth*, 103(B12): 30131–30145, 1998. doi: 10.1029/98jb02302.

Pollitz, F. F. Coseismic Deformation From Earthquake Faulting On A Layered Spherical Earth. *Geophysical Journal International*, 125(1):1–14, 1996. doi: 10.1111/j.1365-246x.1996.tb06530.x.

Roeloffs, E. Tidal calibration of Plate Boundary Observatory borehole strainmeters: Roles of vertical and shear coupling. *Journal of Geophysical Research: Solid Earth*, 115(B6), 2010. doi: 10.1029/2009jb006407.

Scognamiglio, L., Tinti, E., and Quintiliani, M. Time Domain Moment Tensor (TDMT) [Data set]. Istituto Nazionale di Geofisica e Vulcanologia (INGV), 2006. doi: 10.13127/TDMT.

Segall, P., Jónsson, S., and Ágústsson, K. When is the strain in the meter the same as the strain in the rock? *Geophysical Research Letters*, 30(19), 2003. doi: 10.1029/2003gl017995.

Sun, W., Okubo, S., Fu, G., and Araya, A. General formulations of global co-seismic deformations caused by an arbitrary dislocation in a spherically symmetric earth model-applicable to deformed earth surface and space-fixed point. *Geophysical Journal International*, 177(3):817–833, 2009. doi: 10.1111/j.1365-246x.2009.04113.x.

Tamura, Y. and Agnew, D. Baytap08 User's Manual, 2008. https://escholarship.org/uc/item/4c27740c.

Tamura, Y., Sato, T., Ooe, M., and Ishiguro, M. A procedure for tidal analysis with a Bayesian information criterion. *Geophysical Journal International*, 104(3):507–516, 1991. doi: 10.1111/j.1365-246x.1991.tb05697.x.

Valoroso, L., Chiaraluce, L., Di Stefano, R., and Monachesi, G. Mixed-Mode Slip Behavior of the Altotiberina Low-Angle Normal Fault System (Northern Apennines, Italy) through High-Resolution Earthquake Locations and Repeating Events. *Journal of Geophysical Research: Solid Earth*, 122(12), 2017. doi: 10.1002/2017jb014607.

Vuan, A., Brondi, P., Sugan, M., Chiaraluce, L., Di Stefano, R., and Michele, M. Intermittent Slip Along the Alto Tiberina Low-Angle Normal Fault in Central Italy. *Geophysical Research Letters*, 47 (17), 2020. doi: 10.1029/2020gl089039.

Wang, C.-Y. and Barbour, A. J. Influence of pore pressure change on coseismic volumetric strain. *Earth and Planetary Science Letters*, 475:152–159, 2017. doi: 10.1016/j.epsl.2017.07.034.

Wells, D. L. and Coppersmith, K. J. New empirical relationships among magnitude, rupture length, rupture width, rupture area, and surface displacement. *Bulletin of the Seismological Society of America*, 84(4):974–1002, 1994. doi: 10.1785/bssa0840040974.

Wessel, P., Luis, J. F., Uieda, L., Scharroo, R., Wobbe, F., Smith, W. H. F., and Tian, D. The Generic Mapping Tools Version 6. *Geochemistry, Geophysics, Geosystems*, 20(11):5556–5564, 2019. doi: 10.1029/2019gc008515.

Wolfe, J. E., Berg, E., and Sutton, G. H. "The change in strain comes mainly from the rain": Kipapa, Oahu. *Bulletin of the Seismological Society of America*, 71(5):1625–1635, 1981. doi: 10.1785/bssa0710051625.

Zhang, Y., Wang, C., Fu, L., Yan, R., and Chen, X. Mechanism of the Coseismic Change of Volumetric Strain in the Far Field of Earthquakes. *Bulletin of the Seismological Society of America*, 107(1): 475–481, 2016. doi: 10.1785/0120160253.